



RESEARCH ARTICLE

Tuning synergy between nickel and iron in Ruddlesden–Popper perovskites through controllable crystal dimensionalities towards enhanced oxygen-evolving activity and stability

Haijuan Zhang¹ | Daqin Guan^{2,3} | Yuxing Gu⁴ | Hengyue Xu⁵  |
Chunchang Wang¹ | Zongping Shao^{3,4}  | Youmin Guo¹

¹School of Materials Science and Technology, Anhui University, Hefei, Anhui, China

²Department of Building and Real Estate, The Hong Kong Polytechnic University, Hung Hom, Hong Kong, China

³WA School of Mines: Minerals, Energy and Chemical Engineering, Curtin University, Perth, Western Australia, Australia

⁴State Key Laboratory of Materials-Oriented Chemical Engineering, Nanjing Tech University, Nanjing, Jiangsu, China

⁵Tsinghua Shenzhen International Graduate School, Tsinghua University, Shenzhen, Guangdong, China

Correspondence

Daqin Guan, Department of Building and Real Estate, The Hong Kong Polytechnic University, Hung Hom 999077, Hong Kong, China.

Email: daqin.guan@polyu.edu.hk

Zongping Shao, State Key Laboratory of Materials-Oriented Chemical Engineering, College of Chemical Engineering, Nanjing Tech University, Nanjing 21800, Jiangsu, China.

Email: shaozp@njtech.edu.cn

Youmin Guo, School of Materials Science and Technology, Anhui University, No. 111 Jiulong Rd, Hefei 230601, Anhui, China.

Email: yuminguo@ahu.edu.cn

Funding information

Guangdong Basic and Applied Basic Research Foundation, Grant/Award Number: 2023A1515012878; Natural Science Foundation of Anhui Province, Grant/Award Number: 2008085ME134; Australian Research Council Discovery Projects, Grant/Award Numbers: ARC DP200103315, ARC DP200103332; Major Special Science and Technology Project of

Abstract

Ni–Fe-based oxides are among the most promising catalysts developed to date for the bottleneck oxygen evolution reaction (OER) in water electrolysis. However, understanding and mastering the synergy of Ni and Fe remain challenging. Herein, we report that the synergy between Ni and Fe can be tailored by crystal dimensionality of Ni, Fe-contained Ruddlesden–Popper (RP)-type perovskites $(\text{La}_{0.125}\text{Sr}_{0.875})_{n+1}(\text{Ni}_{0.25}\text{Fe}_{0.75})_n\text{O}_{3n+1}$ ($n = 1, 2, 3$), where the material with $n = 3$ shows the best OER performance in alkaline media. Soft X-ray absorption spectroscopy spectra before and after OER reveal that the material with $n = 3$ shows enhanced Ni/Fe–O covalency to boost the electron transfer as compared to those with $n = 1$ and $n = 2$. Further experimental investigations demonstrate that the Fe ion is the active site and the Ni ion is the stable site in this system, where such unique synergy reaches the optimum at $n = 3$. Besides, as n increases, the proportion of unstable rock-salt layers accordingly decreases and the leaching of ions (especially Sr^{2+}) into the electrolyte is suppressed, which induces a decrease in the leaching of active Fe ions, ultimately leading to enhanced stability. This work provides a new avenue for rational catalyst design through the dimensional strategy.

This is an open access article under the terms of the [Creative Commons Attribution](https://creativecommons.org/licenses/by/4.0/) License, which permits use, distribution and reproduction in any medium, provided the original work is properly cited.

© 2023 The Authors. *Carbon Energy* published by Wenzhou University and John Wiley & Sons Australia, Ltd.

Anhui Province, Grant/Award Number: 202103a07020007; Key Research and Development Program of Anhui Province, Grant/Award Number: 202104a05020057

KEYWORDS

crystal dimensionalities, oxygen evolution reaction, Ruddlesden–Popper perovskites, synergy

1 | INTRODUCTION

With the aggravation of the global greenhouse effect, there is an urgent need to seek clean energy sources.^{1,2} Among many low-carbon energy sources, hydrogen is considered as an ideal green energy fuel due to its high energy density and carbon-free nature.^{3,4} Alkaline water electrolysis ($2\text{H}_2\text{O} \rightarrow 2\text{H}_2 + \text{O}_2$) is expected to be one of the most promising hydrogen production technologies in the future.⁵ However, the oxygen evolution reaction (OER) at the anode is a complex four-electron transfer oxidation process ($4\text{OH}^- \rightarrow \text{O}_2 + 2\text{H}_2\text{O} + 4\text{e}^-$), hindering the overall efficiency of water splitting.^{6–8} Although noble-metal oxides (e.g., IrO_2 and RuO_2) have been widely recognized as state-of-the-art OER electrocatalysts, their scarcity and high cost severely hamper large-scale commercial applications.^{9,10} Therefore, the use of cost-effective, active, and stable nonprecious OER catalysts is of paramount importance.

In alkaline solutions, Ni–Fe-based oxides/oxyhydroxides are considered as the most promising nonnoble metal-based electrocatalysts for OER.^{11–16} Numerous studies have demonstrated that the physicochemical properties of Ni–Fe-based oxides/oxyhydroxides can be modified by adjusting the stoichiometry of Ni and Fe ions in the catalyst, thus changing its catalytic activity.^{11,17,18} Forslund et al.¹⁹ tuned charge-transfer interactions by controlling the ratio of Ni to Fe in $\text{La}_{0.5}\text{Sr}_{1.5}\text{Ni}_{1-x}\text{Fe}_x\text{O}_{4\pm\delta}$ oxides to enhance electrocatalytic water splitting. Besides, the synergism at Ni–Fe sites in Ni–FeOOH electrocatalysts can improve Faradaic efficiency and OER dynamics, ultimately resulting in superior catalytic OER activity.¹⁸ Although it has been generally agreed that the coexistence of Ni and Fe elements can boost activity as compared with materials with a single Ni or Fe element, however, most related studies focused on the simple stoichiometric modulation of Ni and Fe ions to achieve improved OER performance. As an important structural parameter and a critical carrier for Ni–Fe ions, crystal dimensionality regulation is always ignored. Furthermore, the role of Ni and Fe ions in the OER activity and stability is still controversial. Friebel et al.²⁰ revealed that the Fe site in $\text{Ni}_x\text{Fe}_y\text{OOH}$ shows higher activity than the Ni site. On the contrary, the doping of Fe^{3+} into the NiBi catalyst was reported to promote the formation of Ni^{4+} active sites, which boosts the OER activity.²¹ To date, the debate on the active sites of Ni–Fe-based oxides/oxyhydroxides is still ongoing. Besides, the stability of Ni or Fe elements plays an

important role in OER performance, which has not been systematically explored and studied so far.

Recently, due to the unique layered structure, Ruddlesden–Popper (RP)-type perovskites have been widely used in solid oxide fuel cells, catalytic NO decomposition and reduction, and room-temperature electrocatalysis.^{22–24} The general formula of RP-type perovskites is $\text{A}_{n+1}\text{B}_n\text{O}_{3n+1}$ ($n = 1, 2, 3, \dots$), where the A site is rare/alkaline-earth-metal cation and the B site is a transition-metal (TM) cation.²³ As shown in Figure 1, along the *c*-axis direction of the crystal unit, the perovskite-like motifs (ABO_3) with *n* layers are situated between the top and bottom rock-salt layers (AO) in the structure of RP-type perovskites. Compared to the conventional three-dimensional simple perovskite, this two-dimensional layered structure provides the best template for modulating the catalytic activity of Ni–Fe-based oxides through crystal dimensionality.^{23,25} In addition, the physicochemical properties of RP-type perovskites can be well modified by tuning the number of perovskite-like layers.^{23,26,27} For example, a Mott insulator–metal transition with a change in bandwidth can be observed in $\text{Sr}_{n+1}\text{Ir}_n\text{O}_{3n+1}$ ($n = 1, 2$, and ∞) as *n* increases.²⁸ Besides, on increasing the number of perovskite-like layers from LaSrNiO_4 ($n = 1$) to $\text{La}_2\text{SrNi}_2\text{O}_{7-\delta}$ ($n = 2$) and further to $\text{La}_3\text{SrNi}_3\text{O}_{10-\delta}$ ($n = 3$), the hybridization strength of Ni 3d–O 2p becomes stronger, leading to enhanced conductivity and improved OER activity.²⁷ Therefore, the flexible crystal dimensionality of RP-type perovskite is highly promising for understanding the relationship between Ni and Fe ions in different dimensions with respect to the OER activity and stability.

Following the above logic, a series of RP-type perovskites ($(\text{La}_{0.125}\text{Sr}_{0.875})_{n+1}(\text{Ni}_{0.25}\text{Fe}_{0.75})_n\text{O}_{3n+1}$ ($n = 1, 2, 3$) with adjustable crystal dimensionality was chosen to investigate the relationship between Ni and Fe ions in different dimensions with respect to OER activity/stability in alkaline solutions. As the dimensionality increases with *n*, the RP-type perovskites show enhanced OER activity and stability. By combining various characterizations, we found that the material with higher dimensionality shows faster reaction kinetics, larger electrochemical active area, and better electron transport capacity (induced by the strengthened Ni/Fe–O covalence). Furthermore, in this RP-type perovskite system, the Fe ions are proven to be the major active sites and the Ni ions to be the key stability sites during the OER process. Besides, as *n* increases, the content

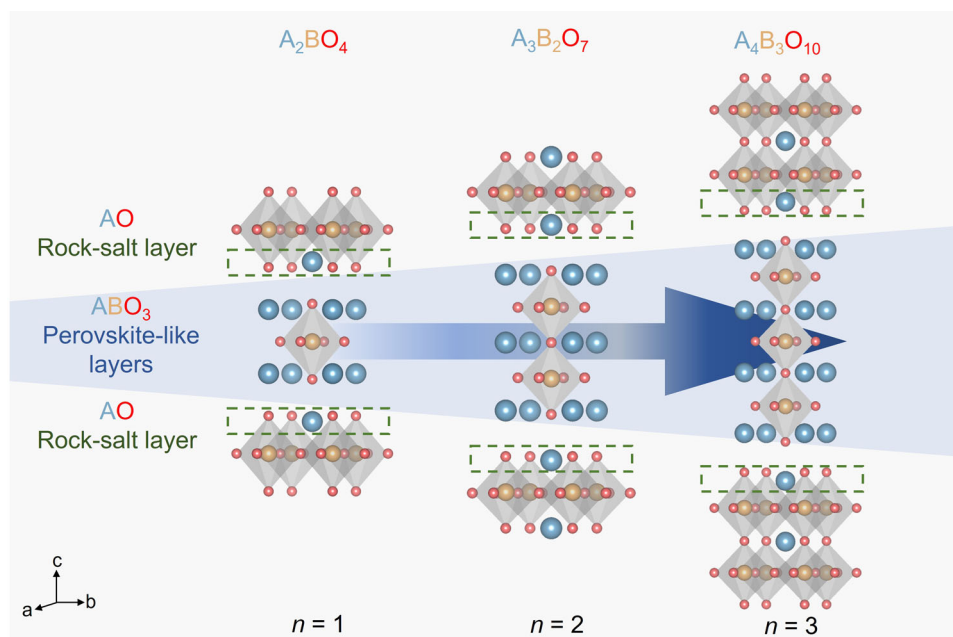


FIGURE 1 Schematic diagram of a tetragonal crystal structure for RP-type perovskites, $A_{n+1}B_nO_{3n+1}$ ($n = 1, 2, 3$).

of unstable rock-salt layers decreases, which is accompanied by a reduction in the leaching of ions. The leaching of A-site ions further triggers the leaching of B-site active Fe ions, while Ni ions are relatively more stable, leading to improved OER stability. We believe that this work will spur further efforts to develop highly active material candidates by crystal dimensionality regulation in a wider range of oxide systems.

2 | EXPERIMENTAL SECTION

2.1 | Catalysts synthesis

LSNF-1, LSNF-2, and LSNF-3 were all prepared using the electrospinning method. Specifically, the corresponding stoichiometric amounts of $\text{La}(\text{NO}_3)_3 \cdot 6\text{H}_2\text{O}$, $\text{Sr}(\text{NO}_3)_2$, $\text{Ni}(\text{NO}_3)_2 \cdot 6\text{H}_2\text{O}$, and $\text{Fe}(\text{NO}_3)_3 \cdot 9\text{H}_2\text{O}$ (all analytical grade; Sinopharm Chemical Reagent Co., Ltd.) were dissolved in 10 mL of *N,N*-dimethylformamide (DMF; Sinopharm Chemical Reagent Co., Ltd.). Then, 1.0 g of polyvinylpyrrolidone (PVP, Mv.1300000; Sinopharm Chemical Reagent Co., Ltd.) was added to DMF, and stirring was continued for 12 h to ensure complete dissolution of the PVP. Subsequently, the above solution was loaded into a 10 mL plastic syringe equipped with a 23-G needle for electrospinning. During the electrospinning process, the voltage was 18 kV and the distance between the aluminum foil collector and the needle tip was set to 10 cm. Finally, the powder catalyst was obtained by calcining the as-collected nanofibers in air at a heating rate of 1°C min^{-1} at 900°C for 2 h.

2.2 | Characterization

X-ray diffraction (XRD) patterns were recorded using a Rigaku Smartlab diffractometer with $\text{Cu K}\alpha$ radiation ($\lambda = 1.5418 \text{ \AA}$), and the structural refinements were revealed using Topas-4.2 software. scanning electron microscopy (SEM) images were obtained using a scanning electron microscope (Hitachi S-4800). High-resolution transmission electron microscopy (HRTEM) images and bright-field transmission electron microscopy (TEM) images were obtained using a transmission electron microscope (FEI Tecnai G2 F20 S-TWIN). The specific surface areas were determined by N_2 adsorption-desorption isotherms on a Quantachrome Autosorb-iQ3 instrument. O 1s X-ray photoelectron spectroscopy (XPS) data were obtained on a Thermo ESCALAB 250Xi instrument. Inductively coupled plasma-mass spectroscopy (ICP-MS) results were obtained on an iCAP 7400 instrument. Specifically, the electrolyte was analyzed by ICP-MS after loading 50 mg of catalysts onto 6 cm^2 of carbon paper and performing 500 OER cyclic voltammetry (CV) scans in a 0.1 M KOH solution.

2.3 | Electrochemical measurements

Electrochemical tests were conducted on a three-electrode electrochemical cell (Pine Research Instrumentation) with an RDE configuration controlled by a CHI 760D electrochemistry workstation. Glassy carbon (GC, 0.196 cm^2), Ag/AgCl, and a graphite rod were used as the working, reference, and counter electrodes, respectively. The catalyst

ink consisted of 10 mg of catalyst, 10 mg of Super P Li, 100 μL of Nafion, and 1 mL of absolute ethanol. Subsequently, 5 μL of catalyst ink was transferred onto the surface of the GC substrate. All polarization curves were recorded at a scan rate of 5 mV s^{-1} from 0.2 to 1.0 V versus Ag/AgCl at a rotation rate of 1600 rpm. Electrochemical impedance spectroscopy (EIS) was recorded from 100 kHz to 0.1 Hz at 0.7 V versus Ag/AgCl under an AC voltage of 10 mV. CV was used to measure the electrochemical double-layer capacitance (C_{dl}). The potential was swept from 0.2 to 0.3 V versus Ag/AgCl at different scan rates of 20, 30, 40, 60, 80, and 100 mV s^{-1} . To measure long-term stability, chronopotentiometry (CP) was recorded at 10 mA cm^{-2} with 0.5 mg of catalysts deposited onto carbon paper (HCP330N; Hanghai Hesen Electric Co., Ltd).

3 | RESULTS AND DISCUSSION

3.1 | Synthesis and characterization of catalysts

First, we synthesized a series of RP-type perovskites by electrospinning, including $\text{La}_{0.25}\text{Sr}_{1.75}\text{Ni}_{0.25}\text{Fe}_{0.75}\text{O}_4$ ($n = 1$, LSNF-1), $\text{La}_{0.375}\text{Sr}_{2.625}\text{Ni}_{0.5}\text{Fe}_{1.5}\text{O}_7$ ($n = 2$, LSNF-2), and

$\text{La}_{0.5}\text{Sr}_{3.5}\text{Ni}_{0.75}\text{Fe}_{2.25}\text{O}_{10}$ ($n = 3$, LSNF-3). To exclude the effect of component ratios between samples of different dimensions, the molar ratio of La ions to Sr ions at the A site is 1:7 and the molar ratio of Ni ions to Fe ions at the B site is 1:3 for all samples. The XRD pattern and the corresponding structural refinement results (Figure 2A–C and Table S1) show that the space groups of LSNF-1, LSNF-2, and LSNF-3 are all $I4/mmm$ with pure phases. To further confirm the structure of RP-type perovskites, we performed HRTEM. As shown in Figure 2D–F, LSNF-1, LSNF-2, and LSNF-3 show lattice stripes of 0.364, 0.264, and 0.278 nm, respectively, corresponding to the respective (011), (112), and (110) crystal planes. Combining XRD refinement patterns and HRTEM patterns, we confirm the successful synthesis of RP-type perovskites by electrospinning with different perovskite-like layers ($n = 1, 2, 3$). Additionally, we further increased n to 4 and ∞ , namely, $\text{La}_{0.625}\text{Sr}_{4.375}\text{Ni-Fe}_3\text{O}_{13}$ ($n = 4$, LSNF-4) and $\text{La}_{0.125}\text{Sr}_{0.875}\text{Ni}_{0.25}\text{Fe}_{0.75}\text{O}_3$ ($n = \infty$, LSNF- ∞), where both form complex multiphase structures (Figure S1), which were not the RP-type perovskites that we needed. Therefore, we selected RP-type perovskites from single (LSNF-1) to double (LSNF-2) to triple (LSNF-3) layers for further investigation.

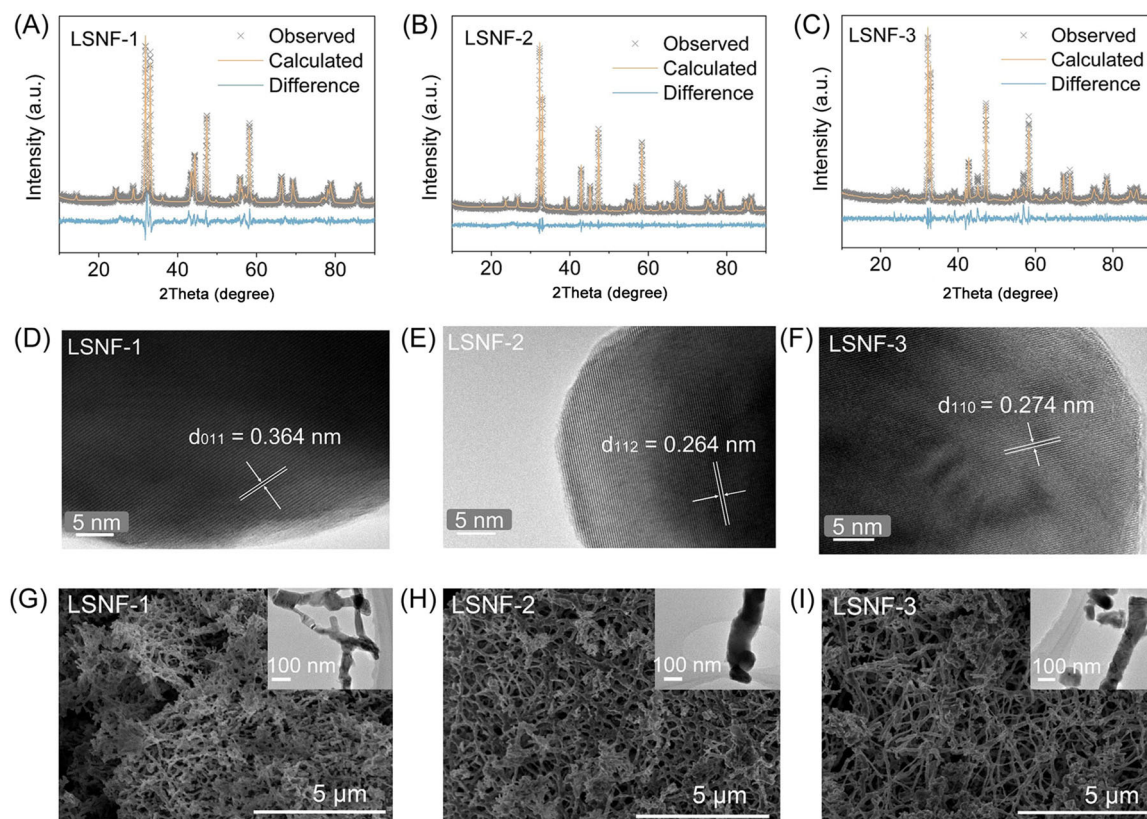


FIGURE 2 Rietveld XRD refinement patterns of (A) LSNF-1, (B) LSNF-2, and (C) LSNF-3. HRTEM images of (D) LSNF-1, (E) LSNF-2, and (F) LSNF-3. SEM images of (G) LSNF-1, (H) LSNF-2, and (I) LSNF-3, where the insets show the bright-field TEM images.

To further demonstrate the microscopic morphology of RP-type perovskites, SEM and bright-field TEM were performed (Figure 2G–I). SEM and bright-field TEM images show that RP-type perovskites with different perovskite-like layers ($n = 1, 2, 3$) all showed the morphology of nanofibers with a diameter of about 100 nm. According to previous research, nanoscale fiber morphology can provide more active sites for catalysts,^{7,29,30} which facilitates the process of OER. The above results show that the RP-type perovskites of different dimensions possessed similar nanofiber morphologies, which allows us to precisely investigate the relationship between catalyst structural dimensionality and OER activity/stability for our purpose.

3.2 | OER performance and activity origins

Next, to evaluate the OER performance of RP-type perovskites, electrochemical tests were carried out on a standard three-electrode system in an O₂-saturated 0.1 M KOH solution, and all voltages were iR-corrected to the reversible hydrogen electrode (RHE) scale (Figure S2). The polarization curves in Figure 3A show that the OER activity was enhanced in the order of LSNF-1 < LSNF-2 < LSNF-3. The LSNF-3 nanofibers require an overpotential of only 360 mV to achieve the current density of 10 mA cm⁻², which is much lower than those of LSNF-1 nanofibers

(448 mV) and LSNF-2 nanofibers (410 mV). Specifically, the OER performance of the LSNF-3 nanofibers is comparable to that of many representative Ni/Fe-based oxide catalysts shown in Table S2, such as La_{*n*+1}Ni_{*n*}O_{3*n*+1} ($n = 1, 2, 3, \infty$)²⁷ and La_{0.5}Sr_{1.5}Ni_{0.7}Fe_{0.3}O₄.¹⁹ Besides, we further analyzed the mass and intrinsic activities of RP-type perovskites with different perovskite-like layers (corrected to the Brunauer–Emmett–Teller surface area; Table S3). As shown in Figure 3B and Table S4, both the mass and the intrinsic activities of LSNF-3 nanofibers are much better than those of LSNF-1 nanofibers and LSNF-2 nanofibers in 0.1 M KOH solution. Specifically, the intrinsic activity of LSNF-3 nanofibers (0.823 mA cm⁻²_{oxide}) at 1.59 V versus RHE is ~10.0 times that of LSNF-1 nanofibers (0.082 mA cm⁻²_{oxide}) and ~4.6 times that of LSNF-2 nanofibers (0.177 mA cm⁻²_{oxide}). The above results demonstrate that the OER performance of RP-type perovskites is greatly enhanced by increasing the number of perovskite-like layers. Next, we will investigate the origins of the activity of LSNF-3 nanofibers.

First, we analyzed the OER kinetics of RP-type perovskites by constructing Tafel curves. In Figure 3C, the Tafel slope decreases from 81.6 mV dec⁻¹ for LSNF-1 nanofibers to 73.6 mV dec⁻¹ for LSNF-2 nanofibers, and further to 68.5 mV dec⁻¹ for LSNF-3 nanofibers, implying that LSNF-3 nanofibers with the highest number of perovskite-like layers show the fastest OER reaction kinetics.³¹ Second, CV was used to further obtain the electrochemical double-layer capacitance (C_{dl}) of

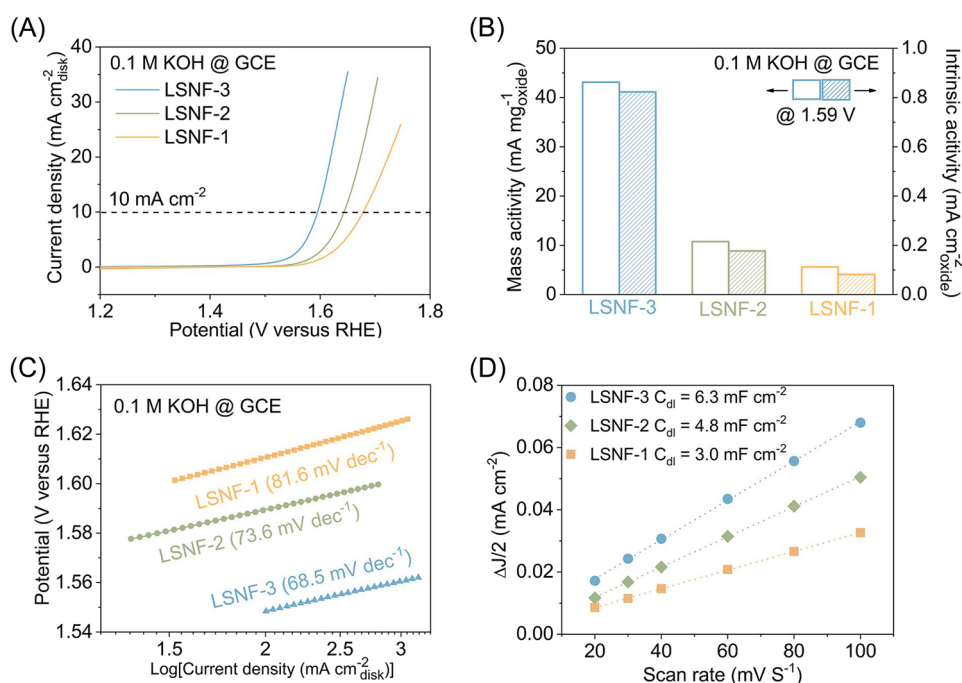


FIGURE 3 (A) OER polarization curves of synthesized oxides. (B) Mass and intrinsic activities of synthesized oxides. (C) Tafel plots of synthesized oxides. (D) Linear fitting of the capacitive currents versus CV scan rates of synthesized oxides.

catalysts (Figure S3), which is positively correlated with the electrochemical effective surface area (ECSA).^{7,32} The C_{dl} value of LSNF-3 nanofibers in Figure 3D is approximately 1.3 and 2.1 times higher than those of LSNF-2 nanofibers and LSNF-1 nanofibers, respectively. The higher C_{dl} value of LSNF-3 nanofibers means that more electrochemical active sites can be generated in the OER process. Meanwhile, it is worth noting that the OER performance of RP-type perovskites, when normalized to the value of ECSA, remains the best performance for LSNF-3 (Figure S4). In addition, we analyzed the O species on the surface of the samples by O 1s XPS. The O 1s spectra in Figure S5 were deconvoluted into four peaks for lattice oxygen (O^{2-}), reactive oxygen species (O_2^{2-}/O^-), hydroxyl groups or surface-adsorbed oxygen (OH^-/O_2), and adsorbed H_2O or carbonate.^{30,33} The results of the O 1s spectra show that the content of O_2^{2-}/O^- species in LSNF-3 nanofibers is the highest, followed by LSNF-2 nanofibers and LSNF-1 nanofibers. The O_2^{2-}/O^- species have been reported to be the active sites in OER.^{34,35} Thus, the high concentration of O_2^{2-}/O^- species for LSNF-3 nanofibers promotes efficient water oxidation. To sum up, with the increase of perovskite-like layers in RP-type perovskites, the catalysts show faster reaction kinetics, larger electrochemical active area, and more active sites (for O_2^{2-}/O^-), ultimately showing better OER activity.

It has been widely reported that the chemical valence state of the oxide surface also plays a crucial role in the OER process.^{33,36,37} In RP-type perovskites, the B-site is the TM ion, which is usually the active site in OER.^{17,30} The A site, on the other hand, is an alkaline earth/rare metal ion with stable valence states and is mainly the coordination environment for the active B–O site.²³ Therefore, we characterized and analyzed the Ni and Fe ions in the B site for RP-type perovskites by soft X-ray absorption spectroscopy (XAS). Soft XAS spectra of the Ni- L_3 and Fe- L_3 absorption edges in total electron yield (TEY) mode are reported to be highly sensitive to the Ni and Fe valence states on the material surface.^{38,39} As shown in Figure 4A, the Ni- L_3 peaks (shaded area) remain essentially unchanged as the number of perovskite-like layers increases, implying that the valence state of Ni ions on the surface of samples is basically stable. In contrast, according to the intensity of the Fe- L_3 peaks (shaded area) in Figure 4B, the peaks of LSNF-1 nanofibers, LSNF-2 nanofibers, and LSNF-3 nanofibers become stronger. According to the Fe- L_3 absorption peak intensities for Fe–O coordination numbers of six-coordinated Fe_2O_3 and four-coordinated $YBaCo_3FeO_7$,⁴⁰ when the intensity of the absorption peak at ~ 707 eV is stronger, the coordination number of Fe–O is higher. Since the valence states of La/Sr ions in the A

site and Ni ions in the B site for RP-type perovskites are stable, the higher Fe–O coordination number in the B site shows increased Fe valence according to the requirement of charge balance. Therefore, the Fe valence in RP-type perovskites becomes higher with increasing perovskite-like layers. Besides, complete iodometric titration experiments were carried out to further confirm the valence order of the B-site ions for RP-type perovskites. Owing to the higher Fe/Ni valence of RP-type perovskites with more perovskite-like layers, the consumption of $Na_2S_2O_3 \cdot 5H_2O$ solutions for LSNF-3 is the highest, followed by LSNF-2 and LSNF-1 (Figure S6).

It is well known that the TM–O covalency also plays a key role in the OER process. Therefore, we performed O-K XAS to study the TM–O covalency of our samples. According to the above soft XAS results, there is almost no difference in the valence of Ni for RP-type perovskites with different perovskite-like layers. Thus, the difference in the covalency of TM–O in the O-K XAS spectrum is mainly a difference in Fe–O covalency. As shown in Figure 4C, the energy position of the O-K pre-edge peak shifts to lower energy positions from LSNF-1 nanofibers to LSNF-2 nanofibers and further to LSNF-3 nanofibers, and the spectrum weight of the O-K pre-edge peak gradually increases from LSNF-1 nanofibers to LSNF-2 nanofibers and then to LSNF-3 nanofibers, which indicates that LSNF-3 nanofibers show the highest Fe–O covalency. Thus, with an increased number of perovskite-like layers, the TM–O covalency increases as the valence of the TM ion increases, which can be demonstrated by the well-known charge-transfer model (Figure 4E).^{4,41} As the number of perovskite-like layers in RP-type perovskites increases from 1 to 2 and further to 3, the charge-transfer energy decreases (the energy difference between the O 2p center and the unoccupied TM 3d center) and the occupied and unoccupied orbitals move towards the Fermi level (E_F), resulting in enhanced density of the orbital electron cloud. Ultimately, it is easier for electrons to jump from the occupied O 2p orbitals to the empty TM 3d orbitals, conferring the best electron transfer and OER performance for $n = 3$.^{4,33} Experimentally, the conductivity of catalysts was further verified by EIS tests. In Figure S7, the EIS spectra are composed of the solution resistance (R_s), the polarization resistance (R_p), and the constant phase element, where the R_p value can reflect the electron transport capacity of the sample.^{4,33} As expected, the R_p value of LSNF-3 nanofibers ($\approx 72 \Omega$) is much lower than that of LSNF-2 nanofibers ($\approx 88 \Omega$) and LSNF-1 nanofibers ($\approx 118 \Omega$), indicating the fastest electron transfer on LSNF-3 nanofibers during OER. The above results indicate that as the number of perovskite-like layers for RP-type perovskites increases, the valence state of Ni ions

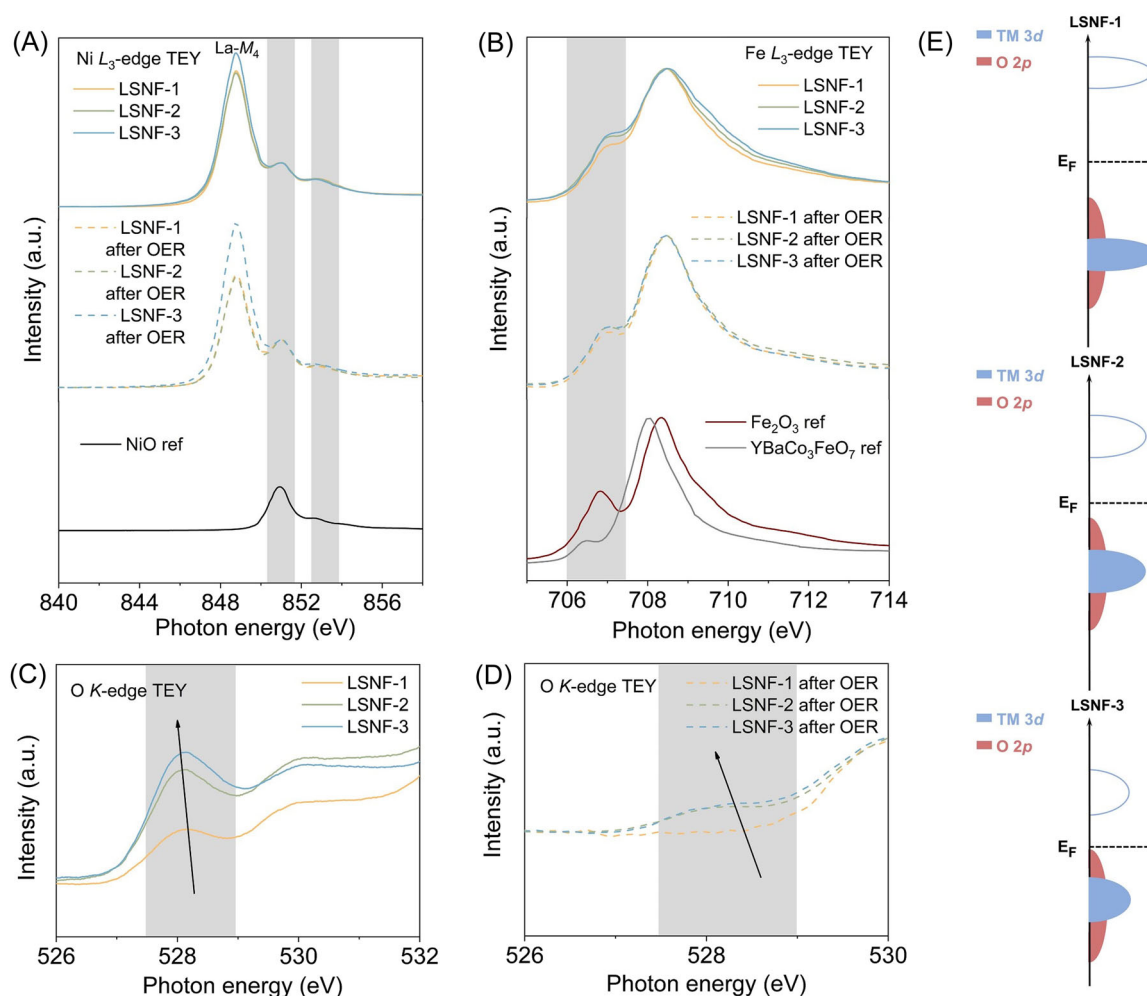


FIGURE 4 (A) Ni- L_3 XAS spectra in TEY mode of synthesized oxides before and after OER and standard samples. (B) Fe- L_3 XAS spectra in TEY mode of synthesized oxides before and after OER and standard samples. O- K XAS spectra in TEY mode of synthesized oxides (C) before and (D) after OER. (E) Charge-transfer model of synthesized oxides.

remains essentially unchanged, while the valence state of Fe ions becomes higher and the Fe-O covalency is enhanced, resulting in higher conductivity and thus higher OER activity for LSNF-3 nanofibers. From the above results, we can infer that Fe ions are the main active sites and Ni ions are the key stability sites in this RP-type perovskite system, which is in agreement with the results of ICP-MS in the study of stability below.

To further investigate the activated active site at the B site for RP-type perovskites, we conducted soft XAS after the OER. As shown in Figure 4A, the valence state of Ni ions remained essentially unchanged after the OER as the number of perovskite-like layers increased. According to the results of the Fe- L_3 spectrum (Figure 4B) after the OER, the valence state of Fe ions remains in the order of LSNF-3 > LSNF-2 > LSNF-1. Meanwhile, according to the O- K XAS spectrum in Figure 4D, the spectrum weight of the O- K pre-edge peak of RP-type perovskites with different perovskite-like layers after the

OER still follows the same order as that before OER. Therefore, we further confirmed that the Fe ions in the B site are the active sites, while the Ni ions are the main stable sites in the OER process.

In summary, with the increase of perovskite-like layers in RP-type perovskites, LSNF-3 nanofibers show higher Fe-ion valence and stronger TM-O covalency, resulting in better electrical conductivity and a more favorable OER process.

3.3 | OER stability and stability origins

In addition to the OER activity, stability is another important concern for energy-conversion technologies. Here, we compared the OER stability of RP-type perovskites with different perovskite-like layers in O_2 -saturated 0.1 M KOH solutions at a current density of 10 mA cm^{-2} by CP tests. As shown in Figure 5A, the overpotential of LSNF-3 nanofibers

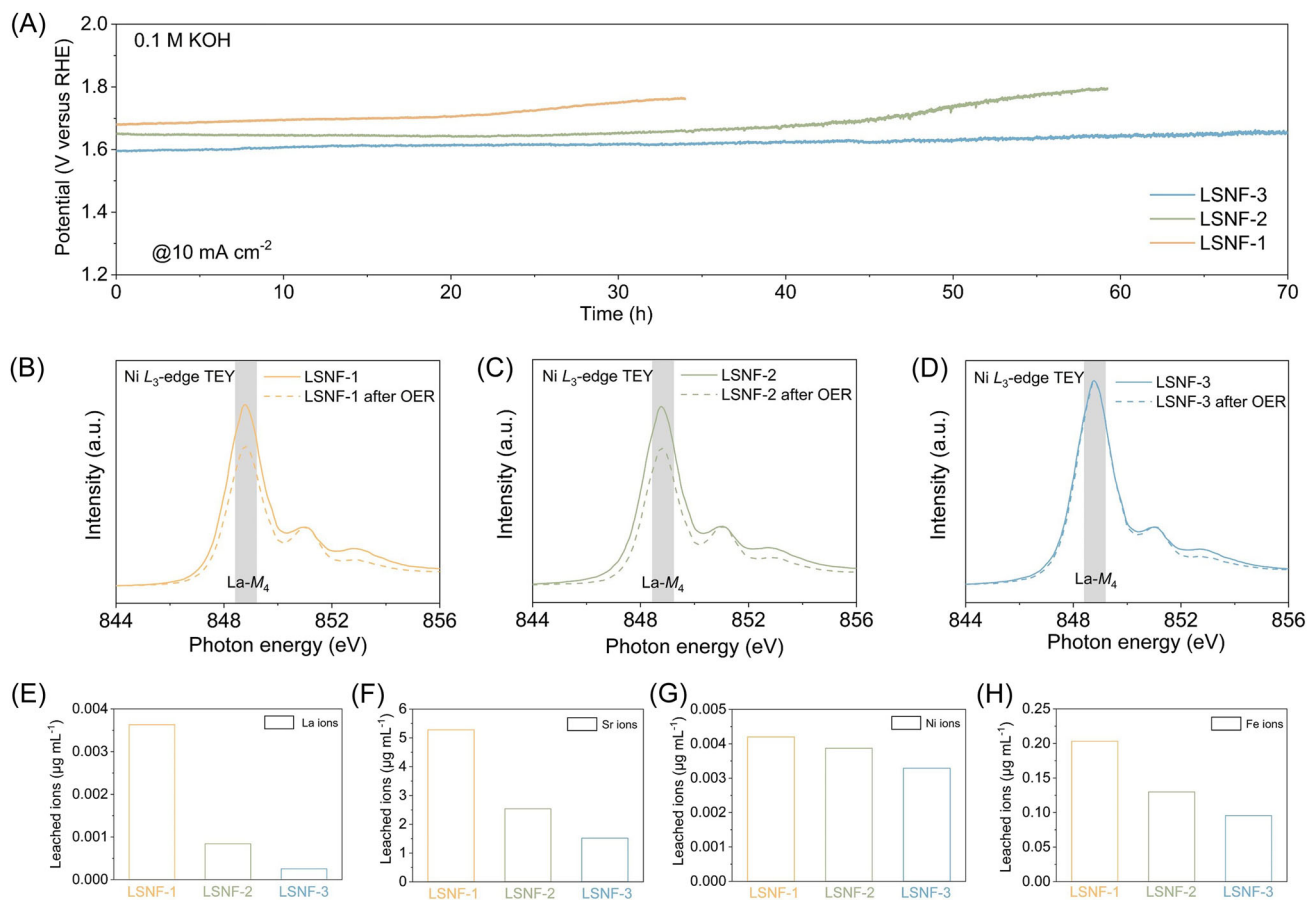


FIGURE 5 (A) Chronopotentiometric curves of synthesized oxides at $10 \text{ mA cm}^{-2}_{\text{disk}}$. Ni- L_3 XAS spectra in TEY mode of (B) LSNF-1, (C) LSNF-2, and (D) LSNF-3 before and after OER. Concentrations of leached (E) La ions, (F) Sr ions, (G) Ni ions, and (H) Fe ions into the solution for LSNF-1, LSNF-2, and LSNF-3.

shows negligible potential changes during the 70 h test, demonstrating excellent stability. However, the overpotentials of LSNF-2 nanofibers and LSNF-1 nanofibers increase significantly after 45 and 20 h, respectively.

To further analyze the origins of the differences in stability in RP-type perovskites with different perovskite-like layers, we conducted soft XAS and ICP-MS measurements after OER. First, we investigated ion leaching of La for RP-type perovskites before and after OER by comparing the intensity of the La- M_4 absorption peak ($\sim 848.8 \text{ eV}$) in the Ni- L_3 XAS spectra. The intensity of the La- M_4 absorption peak becomes weaker when La ions leach into solutions during the OER process. As shown in Figure 5B–D (shaded area), the intensity of the La- M_4 absorption peaks for LSNF-1 nanofibers and LSNF-2 nanofibers decreases significantly after the OER, while the intensity of the La- M_4 absorption peaks for LSNF-3 nanofibers remains essentially unchanged. Soft XAS results indicate that leaching of La ions is more likely to occur in the LSNF-1 and LSNF-2 nanofibers during the OER process, resulting in an unstable crystal structure, while the LSNF-3 nanofibers show a more

stable crystal structure, which is consistent with the results of the above stability test.

Moreover, we further studied ion leaching of all ions in RP-type perovskites under the same conditions of OER activation (500th CV) by ICP-MS. As shown in Figure 5E–H, the leaching of Sr ions at the A site occurs the most in all RP-type perovskites with different perovskite-like layers. The leaching of the A-site ions leads to partial collapse of the crystal structure, because of which leaching of B-site ions is triggered as well. As expected, the active Fe ions leach more readily than the Ni ions at the B site, suggesting that the Ni ions are the stable sites, which is consistent with the above XAS results. In addition, as the number of perovskite-like layers increases, the leaching of Fe ions is suppressed from LSNF-1 nanofibers ($n=1$) to LSNF-2 nanofibers ($n=2$) and further to LSNF-3 nanofibers ($n=3$). The more active Fe ions are leached, the greater the decrease in OER activity of the catalyst, resulting in poor stability. Therefore, the activity of LSNF-3 nanofibers is maintained during the OER process, which is also consistent with the conclusions above. The above results indicate

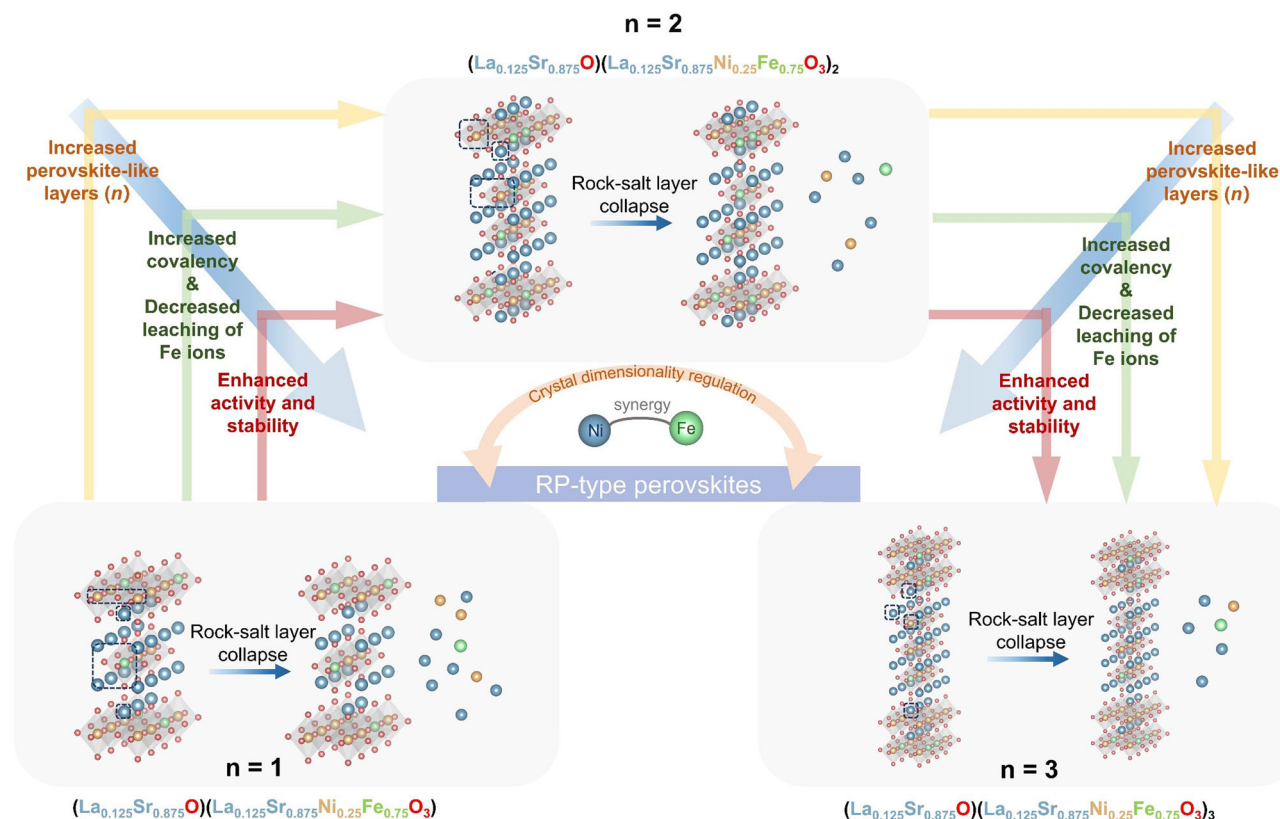


FIGURE 6 Schematic diagram of the relationship between crystal structure and OER activity and stability for RP-type perovskites.

that the crystal structure stability of RP-type perovskites increases with increasing perovskite-like layers.

Above, we have demonstrated that the Fe ions in the B site are the active sites and the Ni ions are the stable sites in this system and that this unique synergy results in the optimal OER performance for $n = 3$. The Ni/Fe–O covalency and leaching of Fe/Ni ions can be modulated through the crystal dimensionality regulation of RP-type perovskites, thus resulting in an increase in the OER activity and stability. Specifically, the crystal structure of RP-type perovskites consists of a rock-salt layer and an n perovskite-like layer alternating with each other, and the unstable rock-salt layer makes the crystal structure prone to collapse during the OER process, which is also consistent with the instability of rock-salt layers in RP-type structures reported in the past.^{7,42} As shown in Figure 6, when n is 1, the content of unstable rock-salt layers in LSNF-1 is high and rock-salt layers are most susceptible to collapse and accompanying leaching of Fe/Ni ions during the OER process, leading to poor activity and stability. As n increases, the number of interconnected perovskite-like layers increases and the number of unstable rock-salt layers decreases. When n is 3, the crystal structure consists of three perovskite-like layers and one rock-salt layer. Although the rock-salt layer is unstable, due to the three perovskite-like layers in LSNF-3,

the overall crystal structure becomes more stable than those of LSNF-1 and LSNF-2. However, when the number of perovskite-like layers continues to increase ($n = 4$ and ∞), the layered structure is not maintained and the resulting composite-phase oxides show poor activity (Figure S8). Besides, as n increases, the content of relatively stable perovskite-like layers increases, allowing for increased Ni/Fe–O covalency and enhanced activity. Therefore, the activity and stability of RP-type perovskites increase with increasing perovskite-like layers, and LSNF-3 shows the best activity and stability during the OER process.

4 | CONCLUSION

In summary, we have successfully improved OER activity/stability by tailoring the synergy of Fe and Ni in RP-type perovskites through structural dimensionality regulation. With the increase of perovskite-like layers, the material with $n = 3$ showed a higher Fe-ion valence and stronger Ni/Fe–O covalency, which significantly enhanced OER activity in alkaline media. Moreover, soft XAS and ICP-MS measurements revealed that the Fe ions are the main active sites and the Ni ions are the main stability sites at the B site in this RP-type perovskite system. As n increases, the number of unstable rock-salt

layers decreases and the leaching of Sr ions at the A site decreases, which induces a decrease in the leaching of active Fe ions at the B site, ultimately leading to an increase in stability. This work not only establishes the relationship between the structure and the activity/stability of RP-type perovskites but also enlightens the design of next-generation high-performance catalysts in terms of dimensional control.

ACKNOWLEDGMENTS

The authors are grateful for the support of the Australian Research Council Discovery Projects under Nos. ARC DP200103332 and ARC DP200103315 (Zongping Shao), the Guangdong Basic and Applied Basic Research Foundation under No. 2023A1515012878 (Daqin Guan), the Major Special Science and Technology Project of Anhui Province under No. 202103a07020007, the Key Research and Development Program of Anhui Province under No. 202104a05020057, and the Natural Science Foundation of Anhui Province under No. 2008085ME134 (Youmin Guo).

CONFLICT OF INTEREST STATEMENT

The authors declare that there are no conflicts of interests.

ORCID

Hengyue Xu  <http://orcid.org/0000-0003-4438-9647>

Zongping Shao  <http://orcid.org/0000-0002-4538-4218>

REFERENCES

- Seh ZW, Kibsgaard J, Dickens CF, Chorkendorff I, Nørskov JK, Jaramillo TF. Combining theory and experiment in electrocatalysis: insights into materials design. *Science*. 2017;355(6321):eaad4998.
- Chu S, Majumdar A. Opportunities and challenges for a sustainable energy future. *Nature*. 2012;488(7411):294-303.
- Wu A, Xie Y, Ma H, et al. Integrating the active OER and HER components as the heterostructures for the efficient overall water splitting. *Nano Energy*. 2018;44:353-363.
- Guan D, Zhang K, Hu Z, et al. Exceptionally robust face-sharing motifs enable efficient and durable water oxidation. *Adv Mater*. 2021;33(41):2103392.
- Fabbri E, Nachtegaal M, Binniger T, et al. Dynamic surface self-reconstruction is the key of highly active perovskite nanoelectrocatalysts for water splitting. *Nat Mater*. 2017;16(9):925-931.
- Wu ZP, Lu XF, Zang SQ, Lou XW. Non-noble-metal-based electrocatalysts toward the oxygen evolution reaction. *Adv Funct Mater*. 2020;30(15):1910274.
- Zhang H, Guan D, Hu Z, et al. Exceptional lattice-oxygen participation on artificially controllable electrochemistry-induced crystalline-amorphous phase to boost oxygen-evolving performance. *Appl Catal B*. 2021;297:120484.
- Huang ZF, Song J, Du Y, et al. Chemical and structural origin of lattice oxygen oxidation in Co-Zn oxyhydroxide oxygen evolution electrocatalysts. *Nat Energy*. 2019;4(4):329-338.
- Guan D, Ryu G, Hu Z, et al. Utilizing ion leaching effects for achieving high oxygen-evolving performance on hybrid nanocomposite with self-optimized behaviors. *Nat Commun*. 2020;11:3376.
- Wang Y, Yan D, El Hankari S, Zou Y, Wang S. Recent progress on layered double hydroxides and their derivatives for electrocatalytic water splitting. *Adv Sci*. 2018;5(8):1800064.
- Trotochaud L, Young SL, Ranney JK, Boettcher SW. Nickel-iron oxyhydroxide oxygen-evolution electrocatalysts: the role of intentional and incidental iron incorporation. *J Am Chem Soc*. 2014;136(18):6744-6753.
- Mahmood A, Yu Q, Luo Y, et al. Controllable structure reconstruction of nickel-iron compounds toward highly efficient oxygen evolution. *Nanoscale*. 2020;12(19):10751-10759.
- Merrill MD, Dougherty RC. Metal oxide catalysts for the evolution of O₂ from H₂O. *J Phys Chem C*. 2008;112(10):3655-3666.
- Smith RDL, Prévot MS, Fagan RD, et al. Photochemical route for accessing amorphous metal oxide materials for water oxidation catalysis. *Science*. 2013;340(6128):60-63.
- Goldsmith ZK, Harshan AK, Gerken JB, et al. Characterization of NiFe oxyhydroxide electrocatalysts by integrated electronic structure calculations and spectroelectrochemistry. *Proc Natl Acad Sci USA*. 2017;114(12):3050-3055.
- Wang J, Gan L, Zhang W, et al. In situ formation of molecular Ni-Fe active sites on heteroatom-doped graphene as a heterogeneous electrocatalyst toward oxygen evolution. *Sci Adv*. 2018;4(3):eaap7970.
- Zhang HT, Guo YH, Xiao Y, Du HY, Zhang MT. Heterobimetallic NiFe cooperative molecular water oxidation catalyst. *Angew Chem Int Ed*. 2023;62(18):e202218859.
- Görlin M, Chernev P, Ferreira de Araújo J, et al. Oxygen evolution reaction dynamics, faradaic charge efficiency, and the active metal redox states of Ni-Fe oxide water splitting electrocatalysts. *J Am Chem Soc*. 2016;138(17):5603-5614.
- Forslund RP, Hardin WG, Rong X, et al. Exceptional electrocatalytic oxygen evolution via tunable charge transfer interactions in La_{0.5}Sr_{1.5}Ni_{1-x}Fe_xO_{4+δ} Ruddlesden-Popper oxides. *Nat Commun*. 2018;9:3150.
- Friebel D, Louie MW, Bajdich M, et al. Identification of highly active Fe sites in (Ni,Fe)OOH for electrocatalytic water splitting. *J Am Chem Soc*. 2015;137(3):1305-1313.
- Li N, Bediako DK, Hadt RG, et al. Influence of iron doping on tetravalent nickel content in catalytic oxygen evolving films. *Proc Natl Acad Sci USA*. 2017;114(7):1486-1491.
- Zhu J, Li H, Zhong L, et al. Perovskite oxides: preparation, characterizations, and applications in heterogeneous catalysis. *ACS Catal*. 2014;4(9):2917-2940.
- Xu X, Pan Y, Zhong Y, Ran R, Shao Z. Ruddlesden-Popper perovskites in electrocatalysis. *Mater Horizons*. 2020;7(10):2519-2565.
- Chaianansutcharit S, Hosoi K, Hyodo J, Ju YW, Ishihara T. Ruddlesden-Popper oxides of LnSr₃Fe₃O_{10-δ} (Ln = La, Pr, Nd, Sm, Eu, and Gd) as active cathodes for low temperature solid oxide fuel cells. *J Mater Chem A*. 2015;3(23):12357-12366.
- Liu S, Luo H, Li Y, Liu Q, Luo JL. Structure-engineered electrocatalyst enables highly active and stable oxygen evolution reaction over layered perovskite LaSr₃Co_{1.5}Fe_{1.5}O_{10-δ}. *Nano Energy*. 2017;40:115-121.

26. Huan Y, Chen S, Zeng R, et al. Intrinsic effects of Ruddlesden-Popper-based bifunctional catalysts for high-temperature oxygen reduction and evolution. *Adv Energy Mater.* 2019;9(29):1901573.
27. Cao C, Shang C, Li X, et al. Dimensionality control of electrocatalytic activity in perovskite nickelates. *Nano Lett.* 2020;20(4):2837-2842.
28. Moon SJ, Jin H, Kim KW, et al. Dimensionality-controlled insulator-metal transition and correlated metallic state in 5d transition metal oxides $\text{Sr}_{n+1}\text{Ir}_n\text{O}_{3n+1}$ ($n = 1, 2, \text{ and } \infty$). *Phys Rev Lett.* 2008;101(22):226402.
29. Li T, Lv Y, Su J, et al. Anchoring CoFe_2O_4 nanoparticles on N-doped carbon nanofibers for high-performance oxygen evolution reaction. *Adv Sci.* 2017;4(11):1700226.
30. Hua B, Li M, Zhang YQ, Sun YF, Luo JL. All-in-one perovskite catalyst: smart controls of architecture and composition toward enhanced oxygen/hydrogen evolution reactions. *Adv Energy Mater.* 2017;7(20):1700666.
31. Guan D, Shi C, Xu H, et al. Simultaneously mastering operando strain and reconstruction effects via phase-segregation strategy for enhanced oxygen-evolving electrocatalysis. *J Energy Chem.* 2023;82:572-580.
32. Hona RK, Ramezanipour F. Remarkable oxygen-evolution activity of a perovskite oxide from the $\text{Ca}_{2-x}\text{Sr}_x\text{Fe}_2\text{O}_{6-\delta}$ series. *Angew Chem Int Ed.* 2019;58(7):2060-2063.
33. Zhang H, Gao Y, Xu H, et al. Combined corner-sharing and edge-sharing networks in hybrid nanocomposite with unusual lattice-oxygen activation for efficient water oxidation. *Adv Funct Mater.* 2022;32(45):2207618.
34. Wang X, Pan Z, Chu X, et al. Atomic-Scale insights into surface lattice oxygen activation at the spinel/perovskite interface of $\text{Co}_3\text{O}_4/\text{La}_{0.3}\text{Sr}_{0.7}\text{CoO}_3$. *Angew Chem Int Ed.* 2019;58(34):11720-11725.
35. Liu R, Liang F, Zhou W, Yang Y, Zhu Z. Calcium-doped lanthanum nickelate layered perovskite and nickel oxide nano-hybrid for highly efficient water oxidation. *Nano Energy.* 2015;12:115-122.
36. Guan D, Zhou J, Huang YC, et al. Screening highly active perovskites for hydrogen-evolving reaction via unifying ionic electronegativity descriptor. *Nat Commun.* 2019;10:3755.
37. Hwang J, Rao RR, Giordano L, Katayama Y, Yu Y, Shao-Horn Y. Perovskites in catalysis and electrocatalysis. *Science.* 2017;358(6364):751-756.
38. Peng L, Yang N, Yang Y, et al. Atomic cation-vacancy engineering of NiFe-layered double hydroxides for improved activity and stability towards the oxygen evolution reaction. *Angew Chem Int Ed.* 2021;60(46):24612-24619.
39. Gao X, Wang J, Zhang D, et al. Hollow NiFe_2O_4 nanospheres on carbon nanorods as a highly efficient anode material for lithium ion batteries. *J Mater Chem A.* 2017;5(10):5007-5012.
40. Guan D, Zhong J, Xu H, et al. A universal chemical-induced tensile strain tuning strategy to boost oxygen-evolving electrocatalysis on perovskite oxides. *Appl Phys Rev.* 2022;9(1):011422.
41. Fujimori A, Bocquet AE, Saitoh T, Mizokawa T. Electronic structure of 3d transition metal compounds: systematic chemical trends and multiplet effects. *J Electron Spectrosc Relat Phenom.* 1993;62(1-2):141-152.
42. Gonell F, Sánchez-Sánchez CM, Vivier V, Méthivier C, Laberty-Robert C, Portehault D. Structure-activity relationship in manganese perovskite oxide nanocrystals from molten salts for efficient oxygen reduction reaction electrocatalysis. *Chem Mater.* 2020;32(10):4241-4247.

SUPPORTING INFORMATION

Additional supporting information can be found online in the Supporting Information section at the end of this article.

How to cite this article: Zhang H, Guan D, Gu Y, et al. Tuning synergy between nickel and iron in Ruddlesden-Popper perovskites through controllable crystal dimensionalities towards enhanced oxygen-evolving activity and stability. *Carbon Energy.* 2024;6:e465. doi:10.1002/cey2.465